Nucleon exchange in the absence of strong driving forces: The reaction $^{238}U+^{48}Ca$ at $E_{lab}=425$ MeV

R. T. de Souza,* W. U. Schröder, J. R. Huizenga, J. Tõke,
S. S. Datta, and J. L. Wile
Department of Chemistry and Nuclear Structure Research Laboratory, University of Rochester, Rochester, New York 14627
(Received 12 August 1988)

Mass number, atomic number, energy, and angular distributions have been measured for the projectile-like fragments from the damped reaction $^{238}U+^{48}Ca$ at $E_{lab}=425$ MeV. Correlations in the measured two-dimensional probability distribution $P(A,Z)$ are discussed along with the general dissipative features of the damped reaction mechanism. The first and second moments of the observed atomic and mass number distributions are compared with those of other asymmetric reaction systems. Although the $^{238}U+^{48}Ca$ system is highly asymmetric, its potential energy surface in the vicinity of the injection point has a nearly zero gradient resulting in a negligible drift in the proton number. The proton drifts observed in reactions of ^{238}U with five different projectiles vary systematically with the potential gradient. The mass and charge data are compared with quantitative predictions by a dynamical reaction model based on nucleon exchange. The theoretical model gives a reasonable account of the mass and charge distributions for the $^{238}U+^{48}Ca$ reaction but fails systematically to predict experimental drifts when the driving forces are large.

I. INTRODUCTION

There is now considerable evidence[1] for a damped heavy-ion reaction mechanism induced by the stochastic exchange of nucleons that is accompanied by the conversion of relative kinetic energy into internal excitation energy. In the transport models developed[2,3] for damped reactions, the dependence of the first moments (centroids) of the atomic and mass number distributions on energy loss illustrates the temporal evolution of the net balance of nucleons transferred in different directions. This average drift of the fragment charge and mass distributions is strongly influenced by the local gradient in the underlying potential energy surface (PES). The second moments (variances) of these distributions reflect the total numbers of nucleons exchanged between the reaction partners, while correlations in the joint neutron-proton probability distribution are results of curvature and alignment of the PES in the (N,Z) plane.

The present study of the reaction $^{238}U+^{48}Ca$ at $E_{lab}/A=8.5$ MeV/nucleon was initiated as part of a comprehensive investigation of the effect of static and dynamic driving forces on the evolution of mass and charge asymmetry in damped reactions. In contrast to other asymmetric systems such as $^{238}U+^{40}Ca$, the local gradient of the driving potential associated with the $^{238}U+^{48}Ca$ reaction is predicted to be rather small. Based on this prediction, and assuming a valid interpretation of the total kinetic energy loss in terms of interaction time and impact parameters, one expects a weak energy-loss dependence of the averages of fragment atomic number and mass distributions from the $^{238}U+^{48}Ca$ reaction, atypical for an asymmetric system. An earlier study[4] of the $^{238}U+^{48}Ca$ system is in accord with these expectations, although the data were taken at a bombarding energy close to the interaction barrier, where already at small kinetic energy losses large fragment deformations develop that complicate the interpretation of the results, and model calculations are not readily available for comparison to data. Due to the small driving forces, the present system offers, in addition, the opportunity to isolate the role of the PES in confining the spreading of mass and charge distributions with increasing energy loss.

The experimental data obtained in this work for the $^{238}U+^{48}Ca$ reaction are contrasted to those of other asymmetric reaction systems such as the $^{238}U+^{40}Ca$ system,[5] since the projectiles have different N/Z ratios and provide, hence, for different gradients of the PES in the vicinity of the injection point. Quantitative comparisons are made to Randrup's dynamical reaction model,[2] where the transport of mass, charge, and energy is mediated by the exchange of nucleons between the two collision partners forming a transient dinuclear system. The model predicts the first and second moments of the proton (Z), neutron (N), and mass (A) number distributions, as well as the excitation energies of the primary fragments. To permit a valid comparison with experimental data to be made, the predicted primary distributions have been subjected to a statistical evaporation calculation assuming an average fragment excitation energy division calculated within the transport model.

In Sec. II the experimental data and techniques as well as the data analysis procedures are discussed. A summary of the results for this reaction has already been reported[6] in a comparison of the reactions $^{238}U+^{40}Ca$, ^{58}Ni and ^{64}Ni studied all at 8.5 MeV/nucleon. The general features of the damped reaction $^{238}U+^{48}Ca$ are elucidated in Sec. III. A brief review of the essentials of the nucleon exchange transport model is given in Sec. IV along with a comparison of the various observed conditional and unconditional moments of the mass number and atomic number distributions with the corresponding theoretical predictions. Conclusions are drawn in Sec. V.

II. EXPERIMENTAL TECHNIQUES AND DATA REDUCTION

The aim of the experiment was to measure the mass, charge, angle, and total kinetic energy loss (E_{loss}) distributions for the damped reaction channel in the interaction of 8.5 MeV/nucleon ^{48}Ca ions with ^{238}U target nuclei. The ^{48}Ca beam was delivered by the Lawrence Berkeley Laboratory SuperHILAC accelerator. The targets were 1.2 mg/cm^2 self-supporting, isotopically enriched ^{238}U foils. Two ΔE-E detector telescopes were employed to measure charge and kinetic energy of projectile-like fragments in the angular interval $20° < \theta_{lab} < 39°$. The transmission detectors used in these experiments ranged in thickness from 13.2 to 14.0 μm. The depletion depth of the stop silicon detectors was 100 μm. In one of the telescopes, ΔE and E detectors were separated by a distance of $\sim$80 cm. This telescope was positioned at a fixed laboratory angle of 30° and subtended a solid angle of 0.25 msr. It provided information on the mass number A of projectile-like fragments via the measurement of the time of flight (TOF) between ΔE and E detectors.

The ΔE silicon detectors were protected from δ electrons by 0.13 μm nickel foils and by the magnetic fields generated by Sm-Co magnets. To provide normalization of the data, two additional silicon detectors at forward angles were used to monitor the Rutherford scattering yields. A standard electronics setup was used as described elsewhere.[7]

A simple data reduction scheme was used to transform the measured ΔE, E, and TOF (or ΔE and E only), event by event, into charge, mass, and kinetic energy (or charge and kinetic energy only) of the detected secondary (post-evaporation) products. This procedure utilized the prescription of Moulton *et al.*[8] to correct the detector response for the so-called pulse height defect and next, the method of Braune and Schwalm[9–11] to transform ΔE to Z scale. From the fragment kinetic energy E and its velocity extracted from the TOF information, the mass of the secondary fragment was deduced. Typical mass and charge resolutions achieved were 0.4 and 0.5 units, respectively, in the Z range of 10 to 25. A multiple-peak, chi-squares fitting routine was employed to deduce the distributions in discrete Z and A values from the measured distributions, which are continuous due to the finite experimental resolution. This procedure has been utilized previously in the analysis of the reaction ^{238}U+^{40}Ca, as detailed elsewhere.[5]

The total kinetic energy loss E_{loss} and c.m. scattering angle were then calculated from two-body kinematics, assuming neutron emission to be the dominant deexcitation mechanism for the reaction primaries. For the ΔE-E telescope, for which no TOF information was available, an average secondary mass for each measured Z value had to be assumed in the c.m. transformation. In the reconstruction of the primary c.m. quantities, an equilibrium sharing of the total excitation energy between the primary fragments was assumed. To the extent that this division should deviate from the actual energy sharing, as deemed probable for low and intermediate energy losses, the E_{loss} scale would have to be modified.

III. EXPERIMENTAL RESULTS

Figures 1 and 2 depict the charge and mass distributions, respectively, of the secondary (post-evaporative) projectile-like products detected in the ΔE-E-TOF telescope at $\theta_{lab} = 30°$, summed over reconstructed kinetic energy losses greater than 20 MeV. As can be seen in Fig. 1, the most probable charge is $Z=20$, that of the projectile itself. Since calculations suggest that Z remains virtually unchanged in the deexcitation of the respective primary product, this observation implies a lack of Z drift in the present reaction. This finding is in contrast to the ^{238}U+^{40}Ca reaction studied earlier, where the most probable Z turned out to be 18. Such a behavior of Z distributions is qualitatively understood in terms of the profile of the underlying PES in the vicinity of the injection point. In the latter case the injection point is located on the rather steep slope of the PES, whereas in the case of the reaction ^{238}U+^{48}Ca studied here, the local PES is relatively flat. As seen from Fig. 2, the ^{238}U+^{48}Ca mass distribution shows an overall drift to smaller masses, although in this case the observed behavior is more difficult to interpret in terms of the PES because of significant sequential evaporation of neutrons.

Figure 3 shows a density plot of the distribution of the projectile-like fragments in the (N,Z) plane, as measured at $\theta_{lab} = 30°$, integrated over kinetic energy losses greater than 20 MeV. The injection point, the bin at $Z=20$, $A=48$ is emphasized in the figure. The dashed line in Fig. 3 indicates the minimum in the PES for different binary fragmentations of the composite nucleus. It should illustrate the general trends expected for the evolution of the primary fragment distribution in A and Z. The solid line, on the other hand, represents the beta-stability valley for the projectile-like fragments which should govern their sequential decay. Obviously, the observed nuclide distribution is aligned with neither the dinuclear PES nor the location of the minimum of the beta-stability valley. The lack of alignment with this latter valley demonstrates that features of the primary fragment distributions are largely preserved throughout the deexcitation process. However, a quantitative separation of the effects of nonequilibrium transport within the

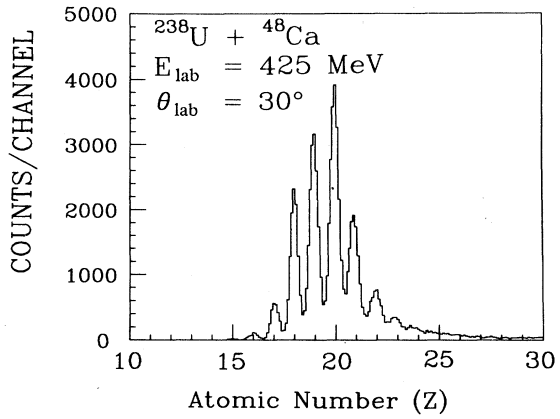

FIG. 1. Experimental atomic number (Z) distribution for all projectile-like fragments with $E_{loss} > 20$ MeV.

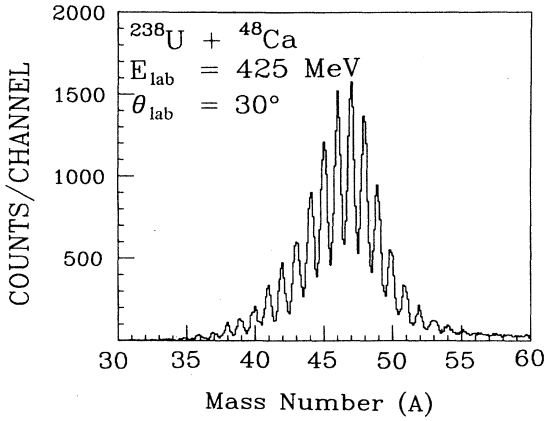

FIG. 2. Observed mass number (A) distribution for all projectile-like fragments with $E_{loss} > 20$ MeV.

dinuclear system from those of sequential decay requires a rather detailed simulation calculation, as discussed further herein. The experimental distribution in Fig. 3 contains mainly neutron-rich nuclides. Among the observed projectile-like fragments are $^{42-44}$Cl, ^{49}Ar, $^{48-50}$K, ^{50,51}Ca, $^{51-53}$Sc, $^{52-54}$Ti, and ^{54,55}V, some of which have already been observed[12] in the reaction ^{238}U+^{56}Fe.

The evolution of the two-dimensional joint probability distribution $P(N,Z)$ with increasing interaction time is portrayed in Fig. 4, where contour plots of $P(N,Z)$ are depicted for the various energy-loss bins indicated in each panel. The degree of total kinetic energy damping represents a measure of the interaction time.[13] The solid and dashed lines in this figure have the same meaning as those of Fig. 3. As seen from Fig. 4, the distribution changes significantly with increasing energy loss (E_{loss}) or interaction time. While for low-energy losses, $P(N,Z)$ is approximately isotropic, strong correlations appear in the distribution at higher values of E_{loss}. With increasing E_{loss}, the distribution rotates and elongates in the direction of the PES valley (dashed line). The data shown in Fig. 4 represent the secondary nuclides, and the evolution of $P(N,Z)$ illustrates, therefore, the balance of the two opposing trends of transport and evaporation. A more quantitative discussion of the energy-loss dependency of the joint probability distribution in terms of orientation angle in the (N,Z) plane and of its width in the direction of its major and minor axes will be given in Sec. IV.

In Fig. 5, projections of the probability distribution are shown for $\theta_{lab}=30°$ and $E_{loss} > 20$ MeV. Here, isotropic differential cross sections $\sigma(A)$ are depicted for various elements from sulfur to vanadium. These elements represent all projectile-like elements formed in the damped reaction with appreciable yields. The cross sections for elements with $Z \leq 20$ decrease smoothly with decreasing Z, and the cross sections for elements $Z < 16$ are very small. This result is to be contrasted with those from the ^{238}U+^{40}Ca reaction,[5] where sizable cross sections were observed for the elements P, Si, Al, Mg, and Na. As seen in Fig. 5, the isotopic distributions of all elements have slight asymmetries, however, without a clear overall trend.

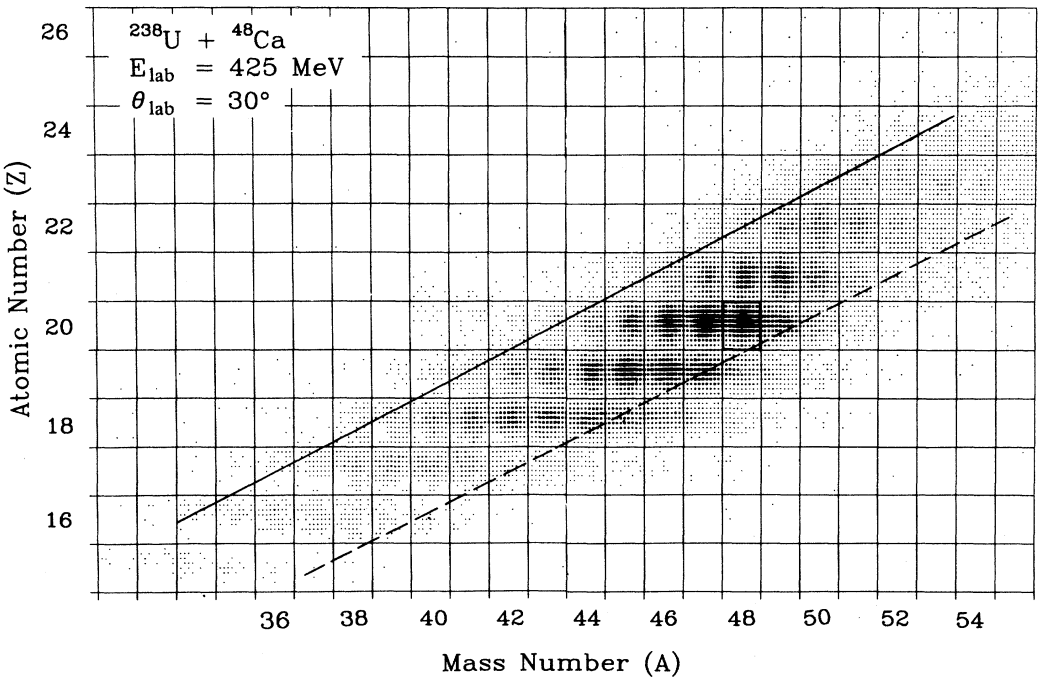

FIG. 3. Population of observed nuclides in the (A,Z) plane represented as a density plot. The injection point is at $Z=28$, $A=48$. The solid line represents the beta-stability line of the projectile-like fragments. The dashed line represents the minimum of the potential energy for the dinuclear system. For all fragments with $E_{loss} > 20$ MeV.

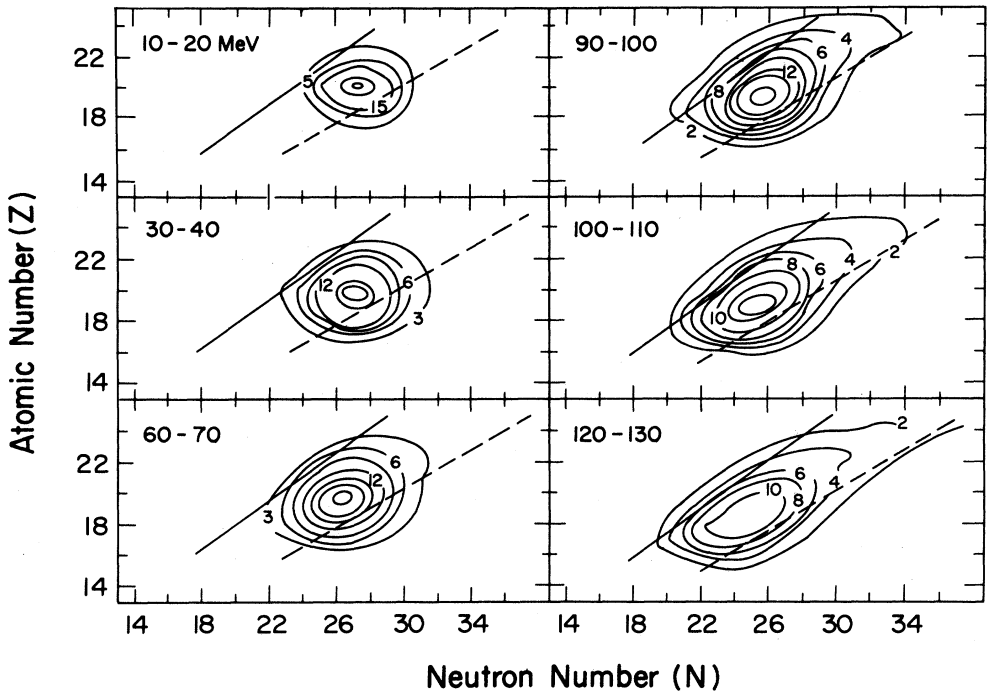

FIG. 4. Evolution of the reaction probability $P(N,Z)$ with E_{loss}. Contours represent levels of constant cross section in arbitrary units. See caption of Fig. 3 for meaning of lines.

In order to establish the several reaction features and to ascertain that the distributions $P(N,Z)$ do not suffer substantially from a bias imposed by the fixed detection angle of $\theta_{lab}=30°$, the angular distributions of the projectile-like fragments were measured using the more efficient (larger solid angle) ΔE-E telescope. The resulting angular distributions for different elements are shown in Fig. 6, whereas two-dimensional representations of these data are given in Figs. 7 and 8. The Wilczyński plot of Fig. 7 depicts contour lines of the double-differential cross section for all Z values vs E_{loss} and $\theta_{c.m.}$ The diffusion diagram of Fig. 8 exhibits contour lines of the angle-integrated double-differential cross section, plotted vs E_{loss} and fragment Z.

As observed from Fig. 6, the angular distributions $d\sigma_{dc}/d\theta_{c.m.}$ for all elements of projectile-like fragments between $Z=15$ and 24 are rather smooth, except for the $Z=20$ distribution showing irregularities caused by instrumental insufficiencies. The distributions are peaked at c.m. angles of approximately 40° and drop exponentially towards larger angles. The relatively small variation of the cross sections $d\sigma_{dc}/d\theta_{c.m.}$ at forward angles is consistent with the orbiting picture[14] for this reaction. This is also inferred from the Wilczyński diagram of Fig. 7. Here, a cross section ridge of damped events evolves from the elastic peak, moving along the E_{loss} axis at an almost constant scattering angle. An indication of an orbiting ridge with rather constant cross sections extending from forward angles is also seen in Fig. 7 for the most damped collisions. This feature is not quite as pronounced as observed[14] in the reaction $^{232}Th+^{40}Ar$.

The dependence of the differential cross section $d^2\sigma/dZdE_{loss}$ on both Z and E_{loss} is shown in Fig. 8 in

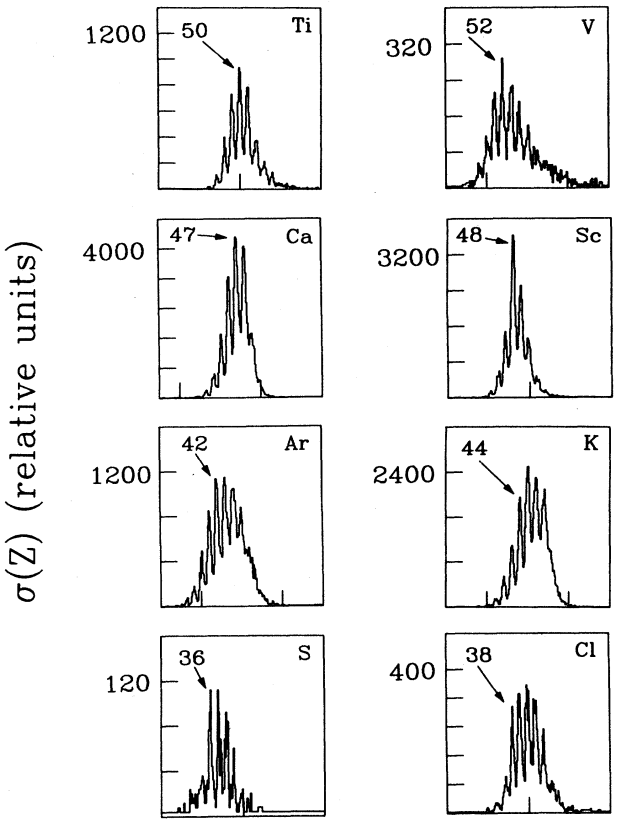

FIG. 5. Mass number distributions of various elements from $Z=16(S)$ to $Z=23(V)$. Arrows identify a prominent mass number in each distribution. The measurements were made at $\theta_{lab}=30°$ for fragments with $E_{loss}>20$ MeV.

the form of a contour diagram, where the isocontours represent lines of constant double-differential cross section in units of $\mu b/(\text{MeV } Z \text{ unit})$. The cross-section ridge is seen to extend parallel to the E_{loss} axis, broadening substantially with increasing energy loss. This feature suggests absence of strong driving forces governing charge transfer between the collision partners. In this respect, the present $^{238}\text{U}+^{48}\text{Ca}$ reaction is rather different from the $^{238}\text{U}+^{40}\text{Ca}$ reaction studied previously,[5] where strong correlations between average fragment Z values and the amount of dissipated energy were observed as indication of substantial underlying driving forces.

In Fig. 9, the cross section of each element for energy losses greater than 20 MeV is plotted versus fragment atomic number in the range $8 \leq Z \leq 27$. This Z distribution is peaked at $Z=20$ and fairly symmetric, quite in contrast to the asymmetric Z distribution measured[5] for the $^{238}\text{U}+^{40}\text{Ca}$ reaction. Projections of the diffusion plot

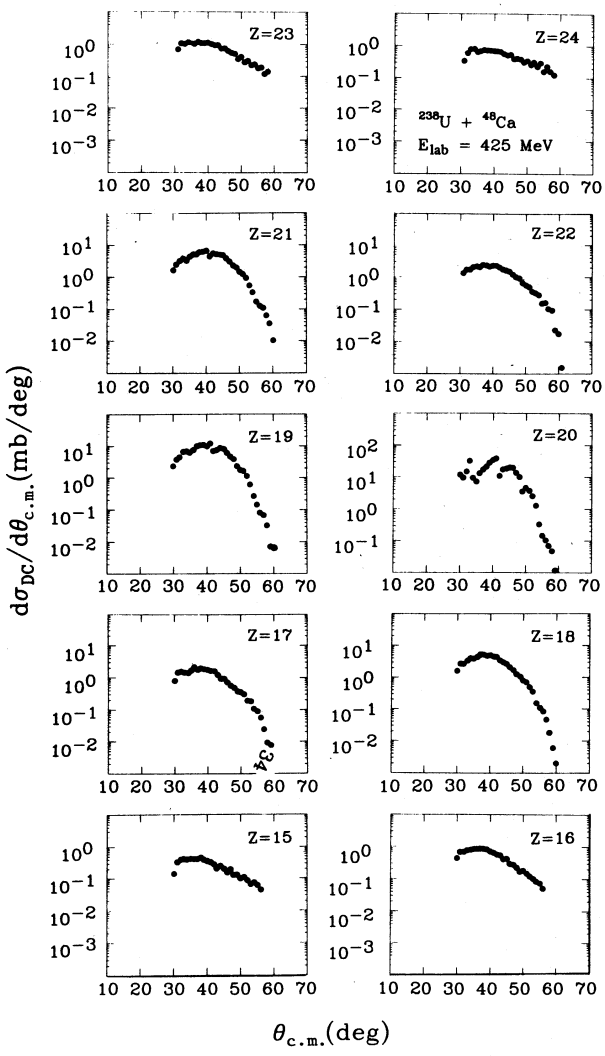

FIG. 6. Center-of-mass angular distributions of projectile-like fragments. The differential cross section $d\sigma_{\text{dc}}/d\theta_{\text{c.m.}}$ (mb/deg) is shown as a function of $\theta_{\text{c.m.}}^{(\text{deg})}$.

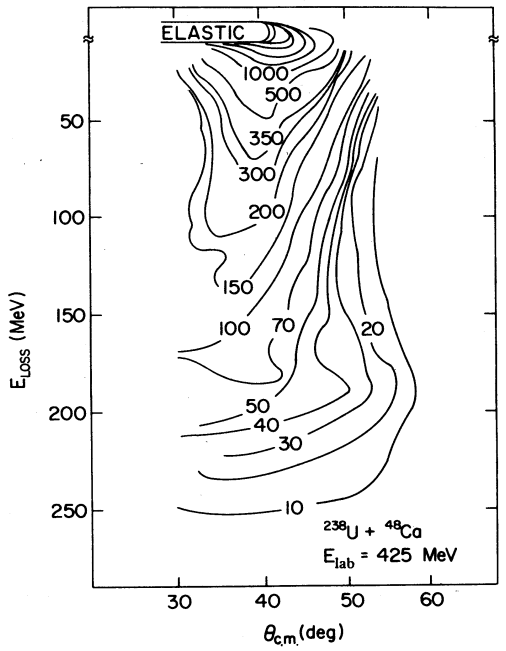

FIG. 7. Wilczyński diagram demonstrating the dependence of the double-differential cross section $d^2\sigma_{\text{dc}}/(d\theta_{\text{c.m.}}dE_{\text{loss}})$ [$\mu b/(\text{deg MeV})$] on both center-of-mass scattering angle ($\theta_{\text{c.m.}}$) and dissipated kinetic energy (E_{loss}).

of Fig. 8, cut at various levels of the energy loss, are exhibited in Fig. 10 showing the Z distributions for twelve different energy-loss bins. Since the collision or interaction time increases with increasing energy loss,[13] the succession of Z distributions depicted in Fig. 10 illustrates the diffusive nature of mass and charge transfer in damped reactions leading to increasingly broader distributions as time proceeds. In spite of a relatively high mobility of the carriers of this diffusion process, the nucleons, there is very little drift of the Z distributions.

The first moment of the Z distributions is rather static at $\langle Z \rangle \simeq 20$, for $E_{\text{loss}} < 100$ MeV, but shifts to slightly

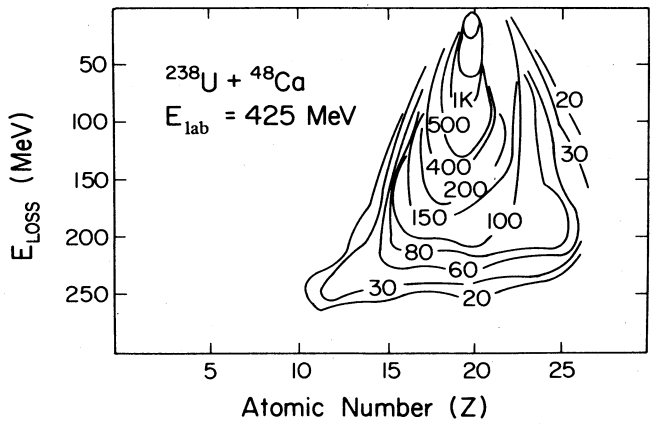

FIG. 8. Contour diagram demonstrating the dependence of the double-differential cross section $d^2\sigma/(dE_{\text{loss}}dZ)$ in units of $\mu b/(\text{MeV } Z \text{ unit})$ on E_{loss} (MeV) and atomic number (Z).

smaller values at higher energy losses. As seen in Fig. 10, the atomic number distributions for energy loss bins of less than $\simeq 100$ MeV are rather symmetric about $Z=20$, quite in contrast to the asymmetric distributions observed for the $^{238}U+^{40}Ca$ reaction.[5]

In Fig. 11 the energy-loss spectra for elements from $Z=17$ to $Z=22$ are plotted for three angular bins centered at $\theta_{c.m.}=35°$, 45°, and 55°, each bin being 10° wide in the center of mass. For $Z=19$, 20, and 21 the quasielastic cross sections at small energy losses are large. In contrast, for $Z=17$ and 18, the cross sections for quasielastic processes are relatively small and the double-differential cross sections peak at larger energy losses. This latter, strongly damped, component is also visible in the $\theta_{c.m.}=55°$ energy-loss spectra for the other elements shown in Fig. 11. The kinematical behavior of this component is consistent with the orbiting picture discussed earlier.

As mentioned before, the preceding distributions, obtained for a wide angular range, were used to establish the extent to which the data measured with the TOF telescope, positioned at a fixed angle of 30°, could be taken as representative for all reaction events. It was found that the bias imposed on these latter data was insignificant for the purposes of this study.

In summarizing the present section, the experimental data from the $^{238}U+^{48}Ca$ reaction at 8.5 MeV/nucleon reveal general dissipative features of damped reactions. As kinetic energy is dissipated, mass and charge distributions broaden. Correlations appear in the joint, two-dimensional probability distributions $P(N,Z)$ which qualitatively reflect the profile of the dinuclear potential energy surface. However, the PES seems to have very little effect on the development of the average of these distributions. As a result of neutron evaporation processes, the (secondary) distributions $P(N,Z)$ show some sensitivity ot the topography of the beta-stability valley.

IV. COMPARISON OF EXPERIMENTAL DATA TO MODEL CALCULATIONS

The stochastic nucleon exchange model due to Randrup[2] will be used in the following for comparisons to experimental data. It has been described in great detail elsewhere and, therefore, only a brief summary of the essentials will be given here. The model is based on a simple microscopic mechanism and makes predictions for a wide range of reaction variables.

According to the model, all dissipative processes

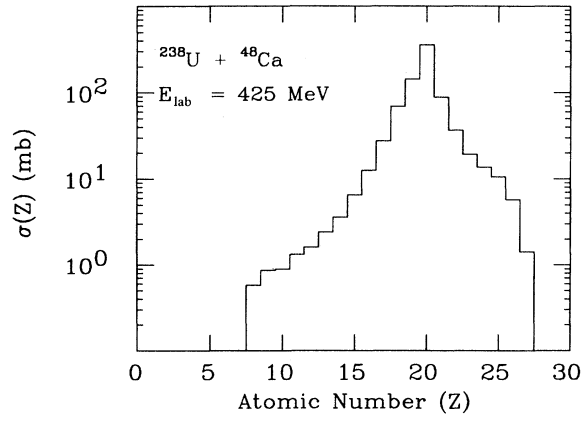

FIG. 9. Cross section of the various elements are shown in units of mb/Z unit versus atomic number (Z) for $E_{loss}>20$ MeV.

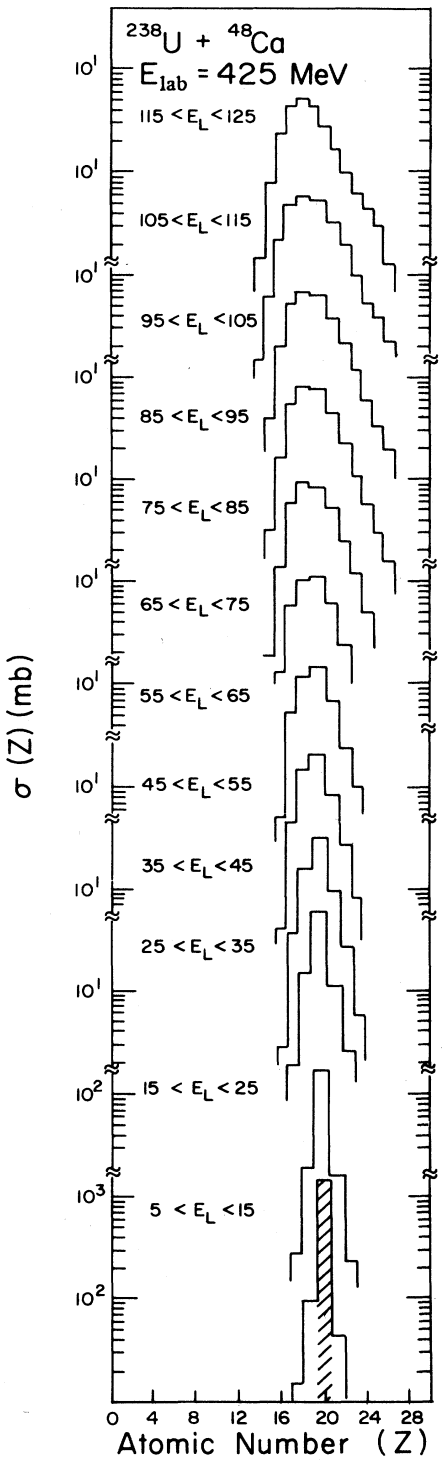

FIG. 10. Evolution of the element distribution for twelve energy-loss bins is portrayed. The cross section for each energy-loss bin in units of mb/Z unit is plotted vs Z.

occurring in strongly damped collisions are the result of a stochastic exchange of nucleons between the two reaction patterns in close proximity. The interacting nuclei form a dumbbell-shaped dinuclear system featuring a cylindrical neck that is fully open for the transfer of nucleons. A set $\{q_i\}$ of macroscopic coordinates is adopted describing the shape of the system, its orientation, its mass and charge asymmetry, as well as the internal state of the constituent fragments. The average values of these coordinates are assumed to follow Lagrange-Rayleigh equations of motion

$$\left[\frac{d}{dt}\frac{\partial}{\partial\dot{\bar{q}}_i}-\frac{\partial}{\partial\bar{q}_i}\right]L=-\frac{\partial}{\partial\dot{\bar{q}}_i}F\ , \tag{1}$$

where the index i runs over all reaction variables. The quantity L is the Lagrangian, and F is the Rayleigh dissipation function. The potential energy is described by

$$V=V_C+V_N+V_P^{LD}+V_T^{LD}-V_0\ . \tag{2}$$

In Eq. (2), the Coulomb potential V_C is calculated for two spherical fragments, according to a prescription given by Bondorf *et al.*[15]

The liquid-drop binding energies, including shell effects, of the target-like and projectile-like fragments are given by V_i^{LD} as calculated by Myers *et al.*[16] The quantity V_0 represents a renormalization constant chosen such that $V=0$ for the configuration of projectile and target nuclei touching at a particular center separation. The nuclear interaction potential is calculated from the surface energy of the dinuclear system and the proximity attraction of juxtaposed surface elements of the spherical fragment outside the neck as

$$V_N(r,\rho)=-2\pi\gamma[\rho^2-\rho(l-l_{\rm geo})]+4\pi\gamma\bar{R}b\Phi(l/b)\exp(-\rho^2/2\bar{R}b)\ . \tag{3}$$

The radius ρ and the length l of the neck are related to each other via the surface separation s,

$$l=s+\frac{\rho^2}{2\bar{R}}\ . \tag{4}$$

Here,

$$\bar{R}=C_1C_2/(C_1+C_2)$$

is the radius of curvature which can be expressed in terms of the half-density radii C_i of the interacting fragments.

The bracket term in Eq. (3) describes the difference between the surface energies of two separated spherical nuclei and that of the dinuclear configuration, whereas the second term represents the proximity attraction. The quantity $l_{\rm geo}$ is a proximity correction to account for that part of the neck already included implicitly in the proximity interaction.[2] The quantities ϕ and b are the proximity form factor and the surface thickness parameter, respectively.

The Rayleigh dissipation function F in Eq. (1) models the conversion of kinetic energy of radial, tangential, and of neck motion into intrinsic heat energy. It is based on mechanisms of exchange of nucleons between the reac-

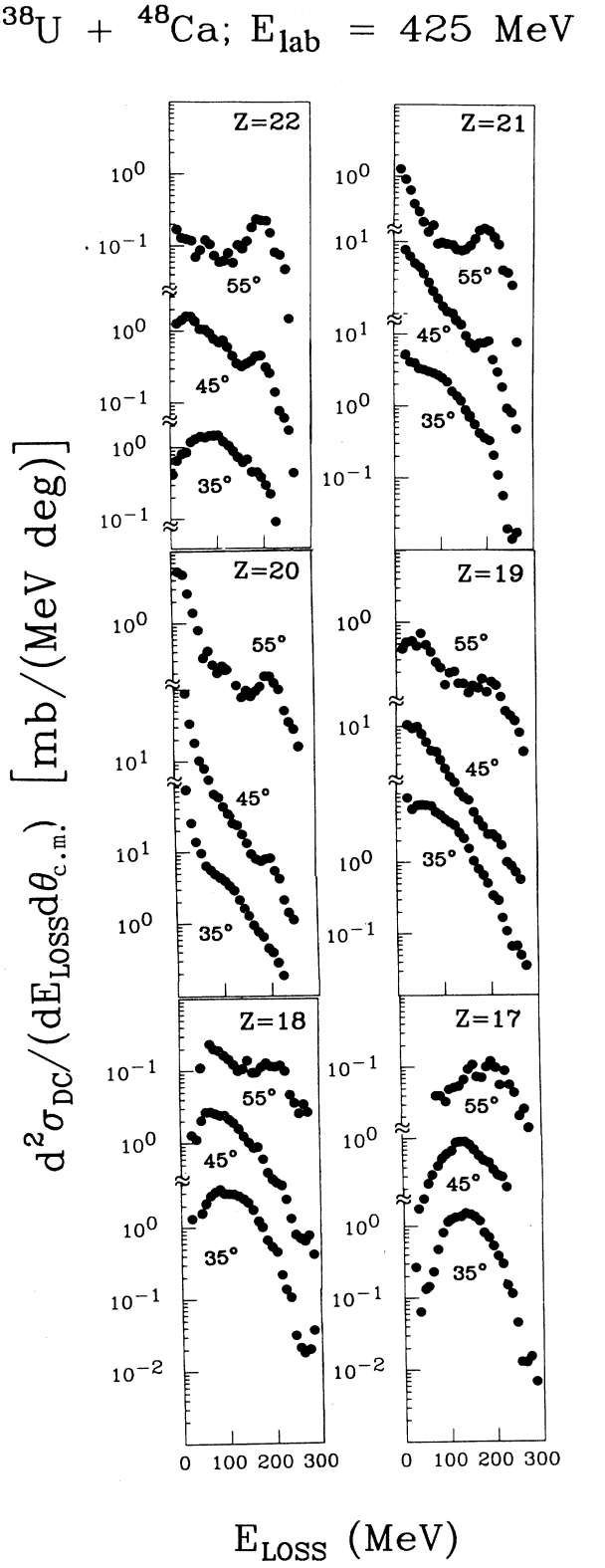

FIG. 11. Kinetic energy spectra are plotted for the various elements ($Z=17$ to $Z=22$). The dependence of the double-differential cross section $d^2\sigma/dE_{\rm loss}d\theta_{\rm c.m.}$ on $E_{\rm loss}$ is shown for three center-of-mass angles.

tion partners ("window friction") and of nucleonic collisions with the moving walls of the neck ("wall friction"). Also contributing to the dissipation of energy are changes in the binding energy resulting from the transfer of nucleons. Consistent with the strong one-body friction forces, motion along the mass and charge asymmetry coordinates, as well as the neck motion are assumed to be overdamped.

In the reaction model, the distributions in the various coordinates about the average trajectories are described by a Fokker-Planck equation. For example, the equation for the fluctuations in neutron and proton number of one of the interaction partners can be written as

$$\frac{\partial}{\partial t}P(N,Z,t)=-\frac{\partial}{\partial N}(v_N P)-\frac{\partial}{\partial Z}(v_Z P)$$
$$+\frac{\partial^2}{\partial N^2}(D_{NN}P)+\frac{\partial^2}{\partial Z^2}(D_{ZZ}P)\ . \qquad (5)$$

Equation (5) describes the time dependence of the joint probability distribution $P(N,Z,t)$ for finding at a given time t, N neutrons, and Z protons in one of the reaction fragments. The quantities v and D represent the drift and diffusion coefficients, respectively. These transport coefficients are calculated[2] microscopically from the instantaneous condition of the dinuclear complex, the constituents of which are always considered to be at their individual thermodynamic equilibria. These coefficients fulfill the generalized Einstein relations

$$v_i=D_{ii}F_i/\tau_i^*,\quad i=N,Z \qquad (6)$$

where F_i represents the dynamical force driving the system along the coordinate i. The quantity τ^* is a measure of the energy interval around the Fermi level involved in nucleon exchange processes.

In the actual numerical calculations, a first-order expansion around the average trajectory is performed to obtain the drift coefficients, and a set of linear coupled equations for the first and second moments of the joint probability P is integrated along the average system trajectory. These transport calculations have been performed with the computer code CLAT developed by Schröder *et al.*[1,17,18] They have been discussed in greater detail elsewhere.[1,17,18]

A cut through the multidimensional PES of Eq. (2) is shown in Fig. 12, where equipotential contour lines are plotted versus neutron number N and proton number Z of one of the interacting fragments. This potential corresponds to the macroscopic energies of all possible binary fragmentations of the composite nucleus ($A=286$, $Z=112$), for a representative angular momentum of $l=175\ \hbar$ and a separation distance of $r=10.74$ fm. This distance represents the classical turning point for the $l=175\ \hbar$ trajectory. Both, shell and proximity effects have been included in the calculation, and the PES is normalized at the injection point marked by a cross in Fig. 12.

The salient features of the PES of Fig. 12 are a deep minimum in the vicinity of $Z=33$, $N=50$, a consequence of strong shell effects in the Pb region experienced by the target-like partners, and a saddle separating this local

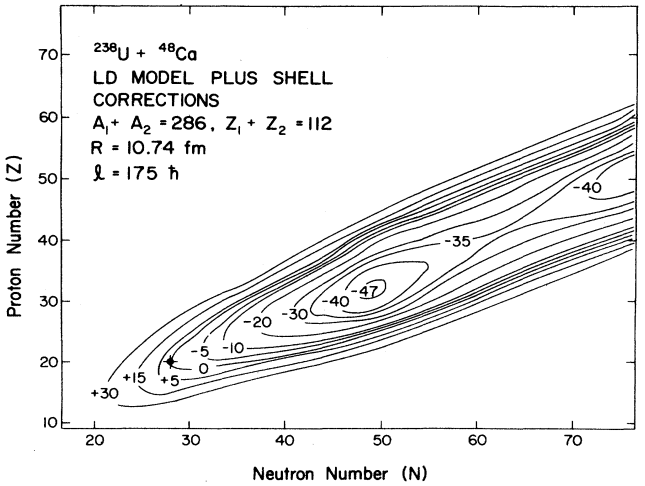

FIG. 12. Contour line representation of the liquid-drop potential surface (with shell and proximity corrections) for all possible binary fragmentations of the composite system $Z=112$, $A=286$.

minimum from the global minimum at symmetric fragmentations. In the vicinity of the injection point, the PES is relatively shallow, compared to the ^{238}U+^{40}Ca system, where the injection point is located on a steep wall of the PES. An alternative representation of the information from the same calculation is illustrated in Fig. 13, showing the vector field of driving forces in the (N,Z) plane around the ^{238}U+^{48}Ca injection point. As can be seen clearly from this figure, the ^{238}U+^{48}Ca system is restrained in the N-Z (isospin) degree of freedom and is predicted to evolve preferentially along the valley of the

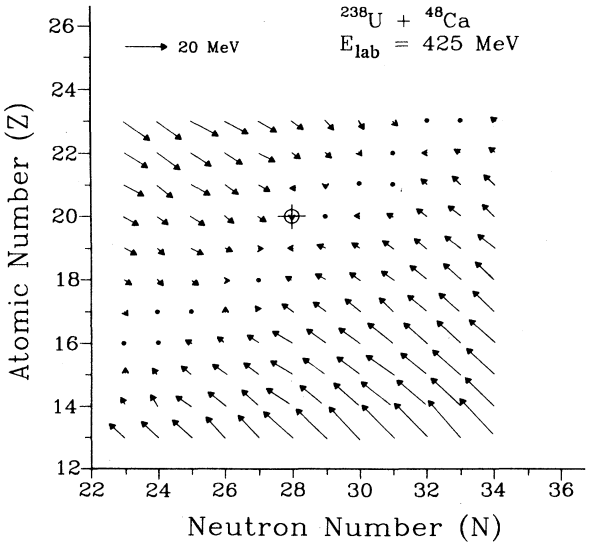

FIG. 13. Driving force $[(\Delta V/\Delta Z)^2+(\Delta V/\Delta N)^2]^{1/2}$ for the transfer of nucleons between the projectile-like and target-like fragments. The length of each arrow denotes the magnitude of the force and the direction indicates the drift direction of the projectile-like fragment.

PES, which is approximately aligned with the direction of $A=N+Z$. Drifts of the joint probability distribution $P(N,Z)$ are expected to be small because of the balance of the driving forces in the injection region, in qualitative agreement with the data discussed in Sec. III. However, the presence of largely different components of the driving forces, related to the curvature of the PES in different directions, should induce characteristic differences in the time evolution of the various second moments of the probability distribution. In the following figures, the data obtained with the TOF telescope will be examined in the light of these considerations and will be compared to quantitative model predictions.

In Fig. 14, the average values of mass, atomic and neutron numbers, offset by the corresponding numbers for the projectile, are plotted versus energy loss. While the triangles represent the present data for the $^{238}U+^{48}Ca$ reactions, data obtained previously for the $^{238}U+^{40}Ca$ reaction are included as dots in Fig. 14 for comparison. These average values correspond to the detected (secondary) projectile-like fragments, a correction due to evaporative effects has only been made in the reconstruction of the kinetic energy loss. As shown by evaporation calculations, the excited primary fragments decay predominantly by neutron evaporation. Hence, the experimentally observed Z distributions reflect mainly the nucleon exchange process and are only slightly distorted by the deexcitation process. Consequently, the observed difference in the experimental data reflect directly the difference in the primary atomic number distributions. Hence, on the average, only a negligible net number of protons is transferred from the projectile-like fragments to the target-like partners, for $E_{\text{loss}} \leq 100$ MeV. In contrast, in the $^{238}U+^{40}Ca$ reaction at $E_{\text{loss}}=100$ MeV, the projectile-like fragment has, on average, transferred 3–4 protons to the heavy reaction partner. For other symmetric systems such as ^{238}U, ^{165}Ho, and $^{209}Bi+^{56}Fe$ at 8.5 MeV/nucleon, it was found[12] that $\langle Z \rangle$ decreases linearly with increasing E_{loss} at a rate of approximately 2.3 ∓ 0.1 units per 100 MeV of E_{loss}. Thus, a striking difference is observed in the E_{loss} dependencies of $\langle Z \rangle$ for the $^{238}U+^{40}Ca$ system on the one hand, and the $^{238}U+^{48}Ca$ system on the other hand. Both types of difference can be attributed to details of the PES affecting the nucleon exchange process. In a recent study, the proton drifts observed in reactions of ^{238}U with five different projectiles was found to vary systematically with the potential gradient.[6]

Model calculations are represented by the curves in Fig. 14. Solid and long-dashed curves correspond to the primary distributions predicted by the transport model. The effects of particle evaporation in the deexcitation of the primary projectile-like fragments are modeled by the statistical evaporation code PACE,[19] yielding the short-dashed and dotted curves in Fig. 14. In these calculations, the primary fragment distributions were those predicted by the dynamical-reaction code CLAT.[1,17,18] Evaporation cascades were then calculated for a sample of the most probable primary products exhausting a large fraction of the total yield. The decay of a large number of primary nuclides with small predicted yields has not been simulated in the evaporation calculation, in order to avoid excessive computer time. This lack of completeness will have to be considered in the interpretation of higher moments of the secondary probability distributions. According to these calculations, the proton evaporation effect is very small for both reactions, whereas neutron and mass numbers can change substantially in neutron evaporation processes. The model gives a good account of the energy-loss dependence of the average mass, neutron and proton numbers of projectile-like fragments from the $^{238}U+^{48}Ca$ reaction. The systematical

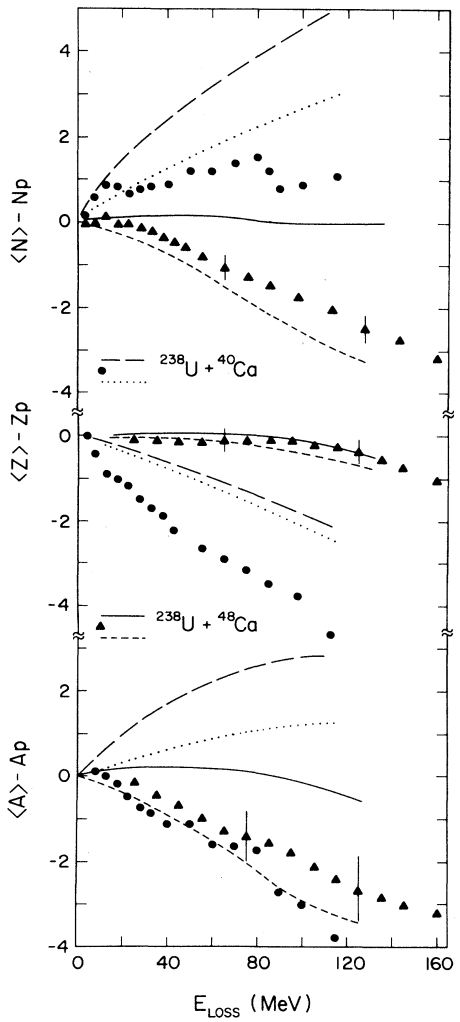

FIG. 14. Mass number drift (average measured atomic mass number minus the mass number of the projectile), proton drift (average measured atomic number minus the atomic number of the projectile), and neutron drift (average neutron number minus the neutron number of the projectile) plotted as a function of energy loss for the $^{238}U+^{40,48}Ca$ reactions. The experimental data (points) and the theoretical predictions (lines) are identified in the figure. The predicted primary distributions (solid and long-dashed lines) are corrected for particle evaporation (short-dashed and dotted lines) with the statistical evaporation code PACE. Representative errors are shown.

effects due to an increased potential gradient can be inferred from a comparison with the $^{238}U+^{40}Ca$ data included in Fig. 14. These effects are qualitatively explained by the transport model, although the model appears to be not sensitive enough to the static driving forces and systematically underpredicts the magnitude ($|\langle Z\rangle - Z_p|$) for the $^{238}U+^{40}Ca$ system, e.g., by approximately 1.5 units at $E_{loss}=100$ MeV.

The quantity ($\langle N\rangle - N_p$), also plotted in Fig. 14, reflects the combined effects of primary neutron exchange processes and sequential evaporation of a significant number of neutrons from the excited primary fragments. Nevertheless, a substantial difference is observed between the reactions induced by the neutron-rich ^{48}Ca projectile and those induced by the ^{40}Ca. The observed change with E_{loss} in the average neutron numbers of projectile-like fragments from the $^{238}U+^{48}Ca$ reaction can almost entirely be understood in terms of the evaporation of increasing numbers of neutrons from primary products with neutron numbers equal to or slightly larger than that of the projectile ^{48}Ca. As seen in the top part of Fig. 14, the transport model predicts primary fragments with $\langle N\rangle - N_p \simeq 0$ (solid curve), due to the small gradient of the PES in the N direction. Corrected for sequential evaporation, the model calculations provide a semiquantitative description of the data. They also predict the proper trend in the development of the average neutron numbers for fragments from the $^{238}U+^{40}Ca$ reaction. Quantitatively, however, the model overpredicts the quantity ($\langle N\rangle - N_p$) for the ^{40}Ca-induced reaction, while it underpredicts this quantity for the reaction $^{238}U+^{48}Ca$. For an energy loss of 100 MeV, discrepancies amount to about one neutron, in either case.

The behavior of the average fragment mass number follows from that of atomic and neutron numbers discussed earlier. It is interesting to note that, while the experimental numbers ($\langle A\rangle - A_p$) decrease with increasing E_{loss} in a rather similar fashion for the two reactions illustrated in Fig. 14, data and calculations show opposing trends, in the case of the $^{238}U+^{40}Ca$ reaction.

Higher moments of the joint probability distributions $P(N,Z)$ are needed, in addition to the first moments discussed earlier, to explore the topography of the underlying PES and its influence on mass and charge transport. Furthermore, the second moments or variances reflect the total numbers of nucleons exchanged stochastically between the collision partners, providing an independent test of the fundamental "window-dissipation" mode assumed[2] in the transport model.

While the evolution of the probability distribution $P(N,Z)$ in the (N,Z) plane has already been presented in Figs. 3 and 4, a more quantitative description of the dependence of the second moments of the Z and N distributions on energy loss E_{loss} is plotted in Fig. 15. The experimentally measured values are represented by solid points, while the solid lines represent the predictions of the dynamical reaction code CLAT.[1,18] As mentioned previously, evaporation corrections have been made to the distributions predicted by the reaction model, in order to deduce moments of theoretical secondary distributions that can be compared to experiments. The arrows

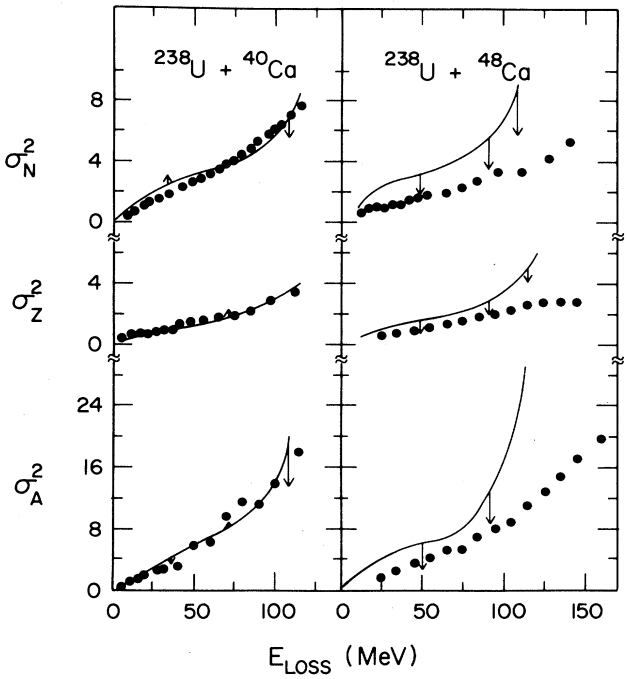

FIG. 15. The variances in the mass number σ_A^2, proton number σ_Z^2, and the neutron number σ_N^2 are plotted as a function of energy loss. The solid lines represent theory uncorrected for particle emission. The arrows indicate the direction and magnitude of the correction to the theoretical variance due to particle evaporation.

on the solid curves in Fig. 15 illustrate direction and magnitude of these corrections, calculated for a few values of E_{loss}, as explained earlier.

In the case of the variances, these estimates should not be taken too literally, since the calculations sample the theoretical primary distributions mostly in the regions of high probability and less extensively in the wings of the probability distribution. This procedure is most appropriate for an evaluation of evaporation corrections for the first moments of the distribution but leads to larger uncertainties in the corrections for the second moments. Keeping these reservations in mind, one finds that in most cases the distributions are narrowed by the evaporation process. Whether evaporation broadens or narrows the distributions depends on the excitation energy division between the reaction partners and the width of the primary N and Z distributions relative to the curvature of the β stability valley. Since the primary neutron variances are approximately double the primary proton variances for both reactions shown in Fig. 15, and the mechanism for the dissipation of kinetic energy is isospin independent, the conclusion is that the number of neutron exchanges is larger than the number of proton exchanges. The theoretical variances, corrected for evaporation, are in relatively good agreement with the data, although the effect of evaporation on the neutron variances for the ^{48}Ca system is relatively large, due to the neutron liability caused by the considerable neutron excess. This agreement indicates that the rate of nucleon

exchange correlates strongly with the energy dissipation rate, consistent with the exchange-induced mechanism assumed in the transport model.

In the following Figs. 16–19, correlations in the joint probability distribution $P(A,Z)$ are examined quantitatively, as a function of energy loss or interaction time. For example, the lower half of Fig. 16 shows the dependence of the ratio of the first moment of the mass and proton number distributions, $\langle A \rangle / \langle Z \rangle$, on energy loss E_{loss}. The experimental data are represented by solid points. The solid line corresponds to the prediction of the dynamical reaction code, while the dashed line represents the theoretical prediction corrected for evaporation. The ratio $\langle A \rangle / \langle Z \rangle$ of the projectile-like fragments for the $^{238}\text{U}+^{48}\text{Ca}$ system remains relatively constant as a function of energy loss. This behavior is due to the fact that the projectile is very neutron rich and the valley in the potential energy surface (cf. Fig. 12) corresponds to nearly the same A/Z value as the injection point. This results in an experimentally observed evolution of the ratio $\langle A \rangle / \langle Z \rangle$ that is governed mostly by evaporation effects. The theoretical prediction corrected for evaporation is in relatively good agreement with the observed data.

The upper half of Fig. 16 shows the dependence of the measured ratio σ_A^2/σ_Z^2 on E_{loss}. In a simple model of uncorrelated diffusion of protons and neutrons, this ratio corresponds to the ratio of the number of nucleons exchanged between the two heavy ions to the number of protons exchanged. For a constant charge density throughout the dinuclear volume, one would then expect[1] this ratio to be given by the ratio of total A to total Z of the system, i.e., $\sigma_A^2/\sigma_Z^2 = A_{\text{tot}}/Z_{\text{tot}} = 2.55$. For a totally correlated statistical exchange, this ratio should be given by the square of the total A/Z ratio, i.e., $\sigma_A^2/\sigma_Z^2 = 6.52$.

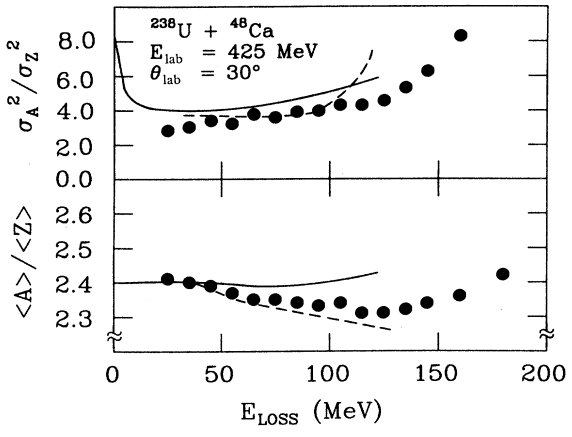

FIG. 16 The lower half of this figure describes the evolution of the ratio $\langle A \rangle / \langle Z \rangle$ with energy loss (E_{loss}). Data are shown by solid points. The solid line depicts the prediction of the classical trajectory code, while the dashed line illustrates the effect of evaporation on the predicted primary distribution. The upper half of the figure shows the dependence of the experimental (solid points) and theoretical (lines) ratios of the variance σ_A^2/σ_Z^2 on E_{loss}.

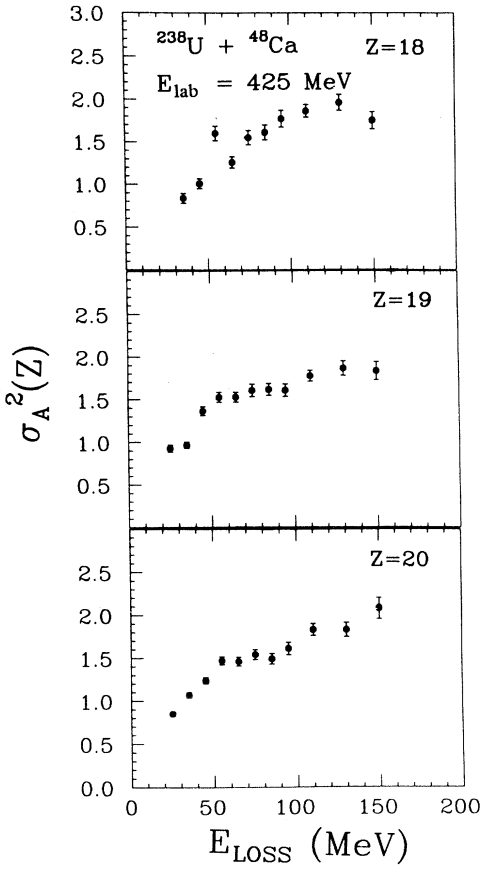

FIG. 17. Isotopic variances (variance in A for fixed Z) for elements $Z=18$, 19, and 20 are shown as a function of E_{loss} (MeV).

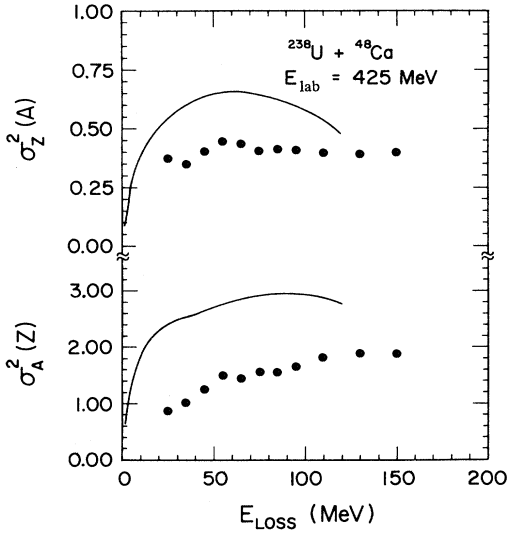

FIG. 18. Isotopic variance (variance in A for fixed Z) and isobaric variance (variance in Z for fixed A) are shown, respectively, in the bottom and top parts of this figure as a function of energy loss. Each data point is averaged over several Z values (bottom) or several A values (top). The theoretical isotopic and isobaric primary distributions are illustrated by the solid lines.

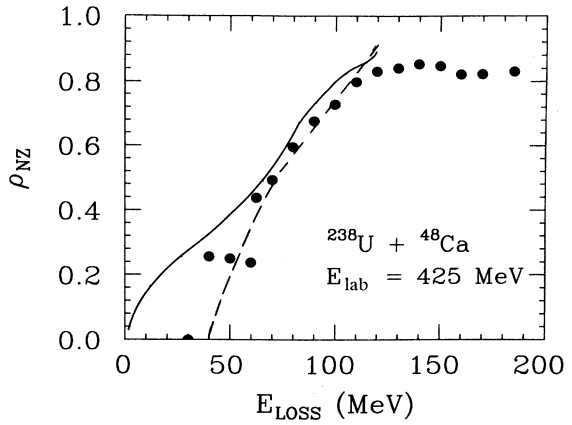

FIG. 19. Behavior of the correlation coefficient ρ_{NZ} with respect to E_{loss} (MeV). The primary and secondary product distributions are represented by solid and dashed lines, respectively.

The experimental ratios shown in Fig. 16 increase from about 3 to 8 with energy losses increasing from 20 to 160 MeV. These values are consistent with observation[1,5,12,20] made for other asymmetric systems and correspond to neither of the above simple limits of correlated or uncorrelated diffusion.

The results of the model calculations for the primary distributions are represented by solid curves in Fig. 16. Dashed curves incorporate estimated corrections due to particle evaporation. Reasonable agreement is reached between the experimental values of σ_A^2/σ_Z^2 and the corrected theory, over a range of energy losses. The large values of σ_A^2/σ_Z^2 for small E_{loss} values associated with peripheral collisions, are, in the model due to the existence of a "neutron skin." In other approaches[21] similar effects of a relatively large neutron mobility arise from the difference in transmission coefficients for neutrons and protons in grazing-type collisions. For larger energy losses, i.e., more penetrating collisions, correlations in the joint probability distribution are enforced due to the curvature and alignment of the PES. This effect is illustrated in Fig. 4, where the distributions are observed to stretch and rotate in the (N,Z) plane with increasing energy loss.

These correlations can be quantified in various different ways. One commonly used method examines the E_{loss} dependence of conditional moments of A and Z distributions, associated with different cuts through the distributions of Fig. 4. As examples, variances of such conditioned distributions are shown in Figs. 17 and 18.

The experimentally measured isotopic variances (variances in A for fixed Z) are displayed in Fig. 17 for the three most populated elements ($Z=18$, 19, and 20) formed in the reaction. All three elements have isotopic variances that increase initially and approximately saturate at energy losses of about 70 MeV and $\sigma_A^2(Z)\simeq 1.8$. The similarity of the isotopic variances of the three elements indicates that the potential energy surface has similar restoring factors for all three of these elements. The isotopic variance averaged over several Z values is compared with theory on the bottom part of Fig. 18. The predictions of the code CLAT correspond to a behavior somewhat similar to the experimental data, although the initial growth appears larger than experimentally observed and theoretical variances saturate at 2.8. Although these corrections are proably not substantial, unfortunately, reliable estimates of evaporation corrections are even more difficult to obtain for conditional variances than for σ_Z^2 and σ_A^2. Hence, the theoretical curves in Fig. 18 correspond to the primary distributions.

The average isobaric variance (variance in Z for a fixed A) is shown as a function of energy loss in the top of Fig. 18. Like the isotopic variance, the isobaric variance is also expected to show initially a quick growth with increasing energy loss, followed by a saturation behavior. However, due to the very strong restoring forces in this degree of freedom, the isobaric variance saturates at a value of approximately 0.4 units in Z. The initial growth to saturation is not measurable due to an insufficient energy resolution and the width of the elastic peak. The dynamical reaction code CLAT overpredicts the magnitude of the isobaric variance as well.

A different method in describing the effect of the PES on the joint probability considers the correlation coefficient ρ_{NZ} and the alignment angle a. The correlation coefficient is defined[1,20] as

$$\rho_{NZ}=\frac{\sigma_{NZ}}{\sigma_N\sigma_Z}\ , \tag{7}$$

in terms of the standard deviations σ_N, σ_Z, and the covariance σ_{NZ}. A value of $\rho_{NZ}=-1$ indicates anticorrelation, whereas $\rho_{NZ}=+1$ indicates full correlation. In Fig. 19 the relationship of the correlation coefficient with the amount of kinetic energy damping is illustrated. The experimental data are shown as solid points, whereas the solid line represents the prediction of the dynamical reaction model. The dashed line corresponds to the correlation coefficient of the secondary distribution predicted theoretically. As can be seen clearly, the data exhibit an almost linear increase with dissipated kinetic energy, until $E_{loss}=100$ MeV. For larger amounts of kinetic energy damping, the experimentally measured correlation coefficient saturates at approximately 0.8. While the theory describes the initial linear increase in the correlation coefficient exceedingly well, the onset of saturation at $E_{loss}=100$ meV observed in the data is not reproduced at this energy loss. Eventually, the theory also predicts a saturation of ρ_{NZ}, however, at a value at which is much closer to 1.0, predicting a full correlation of the proton and neutron nucleon currents.

The tensor of covariances describes a probability ellipsoid, a probability distribution whose contours are ellipses in the (N,Z) plane, as illustrated in the inset at the top of Fig. 20. By a rotation in this plane through an angle[1]

$$a=\tfrac{1}{2}\arctan\left[\frac{2\sigma_{NZ}}{\sigma_N^2-\sigma_Z^2}\right]\ , \tag{8}$$

the ellipsoid can be transformed to principal axes. These "longitudinal" (L) major and "transversal" (T) minor axes represent decoupled degrees of freedom affording in-

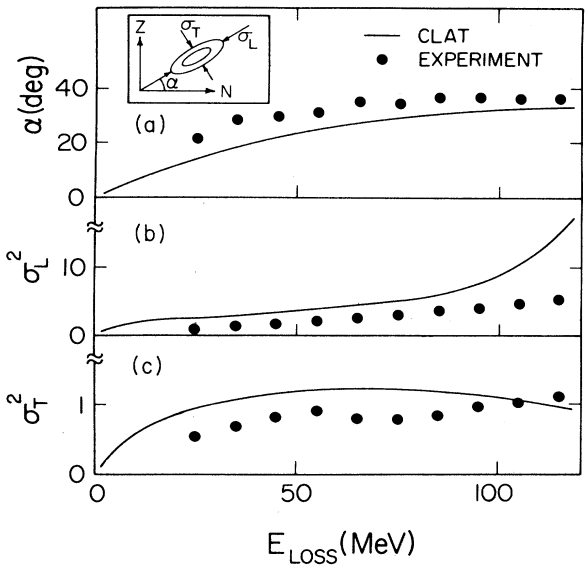

FIG. 20. (a) Angle a of inclination of the probability ellipsoid in the (N,Z) plane vs E_{loss}. The inset shows two schematic contours of this probability distribution and defines rms widths in longitudinal (L) and transversal (T) directions. (b) The variance of the distribution in longitudinal direction is plotted vs E_{loss}. (c) Same as (b) but for the transversal direction.

dependent motion along the corresponding coordinates.

The top portion of Fig. 20 illustrates the results of increasing correlations on the alignment a of the probability ellipsoid. With increasing energy loss, the alignment angle increases, until it levels off at about $a \simeq 36°$. This compares rather well with the angle of inclination a_{PES} of the PES. For example, for the representative PES of Fig. 12, one predicts $a_{PES} \simeq 31°$. The model calculation, illustrated by the solid curve in Fig. 20, reproduces the energy loss or time dependence of the alignment angle semiquantitatively. Correcting for evaporative effects, the theoretical values for a are expected to increase slightly (cf. Fig. 4), improving the agreement between data and calculations.

It is interesting to observe in Fig. 20 the different energy-loss dependencies of the variance σ_L^2 and σ_T^2, which are free of cross correlations ($\sigma_{LT}=0$). Whereas σ_L^2 appears to increase linearly with E_{loss} to about $\sigma_L^2 \simeq 5$, the transverse variance σ_T^2 is much smaller than σ_L^2 and changes by, at most, a factor of 2, over the measured energy-loss range. Such a behavior is consistent with the curvatures of the PES in longitudinal and transversal directions (cf. Fig. 12), which differ approximately by an order of magnitude. Already by relatively small diffusive spreads in the probability distribution, the restoring force due to the PES becomes important enough to prevent any significant further broadening of the probability distribution in this direction. Instead, the mass flow is redirected along the longitudinal coordinate, where the restoring forces are much weaker. As far as the E_{loss} dependence of the variances σ_L^2 and σ_T^2 is concerned, the present results are comparable to those observed[5] for the $^{238}U+^{40}Ca$ reaction, at least at low and intermediate energy losses. For the highest energy losses, the ^{40}Ca-induced reaction leads to somewhat larger variances than the $^{238}U+^{48}Ca$ reaction. Results of the transport model calculation (solid curves in Fig. 20) overestimate both variances σ_L^2 and σ_T^2, for a range of energy losses. Again, proper accounting for evaporation effects is expected to remove some of the discrepancies, as can be concluded from illustrations given in Fig. 15.

V. CONCLUSIONS

The experimental data discussed in the previous sections demonstrate the dissipative character of the reaction $^{238}U+^{48}Ca$. Examination of angular distributions, of the Wilczyński diagram, and of the kinetic-energy spectra of projectile-like fragments indicates an orbiting behavior of the system, although this is not as clearly developed as for other asymmetry systems.

Although the damped reaction $^{238}U+^{48}Ca$ exhibits some general features common to other damped reactions, it also exhibits some rather unique characteristics concerning the behavior of the first moments in proton and neutron number with respect to E_{loss}. These differences are qualitatively understood in terms of the small gradient of the potential energy surface (PES) for the present system. Nevertheless, the differences observed between the $^{238}U+^{40}Ca$ and $^{238}U+^{48}Ca$ reactions are remarkable. By the addition of neutrons alone to a reaction system, the character not only of the fragment neutron and mass number distributions is affected, also the Z distributions change drastically. This change applies to both the average displacement from the injection point and the shape of the fragment charge distributions. While the fragment distributions for the present $^{238}U+^{48}Ca$ reaction are rather symmetric and drift very little with increasing interaction time, those corresponding to the previously studied $^{238}U+^{40}Ca$ reaction exhibit significant asymmetries and show a large drift towards asymmetry, with increasing interaction time.

The effect of the PES on the average drift in fragment Z values is demonstrated in Fig. 21 compiling information on reactions induced by five different projectiles on ^{238}U targets. In Fig. 21, the slopes of $(\langle Z \rangle - Z_p)$ as a function of energy loss, $d(\langle Z \rangle - Z_p)/dE_{loss}$, determined from the more peripheral collisions with energy losses of up to 50 MeV, are plotted versus the gradient dV/dZ of the PES. Each value of the dV/dZ in Fig. 21 is an average value taken around the injection point of a particular reaction, again for energy losses up to 50 MeV. As can be seen from this figure, the slopes in the proton drift correlate rather well with dV/dZ.

Quantitative comparison with a nucleon exchange transport model and evaporation code is relatively successful in reproducing the experimentally observed drift in Z for this reaction, despite failure of the same model to reproduce the quantitative behavior of $\langle Z \rangle$ with respect to E_{loss} for the reaction $^{238}U+^{40}Ca$. Generally good agreement of the theory in reproducing the covariances of the joint probability distribution is an indication of the insensitivity of the second moments to a drastic change in

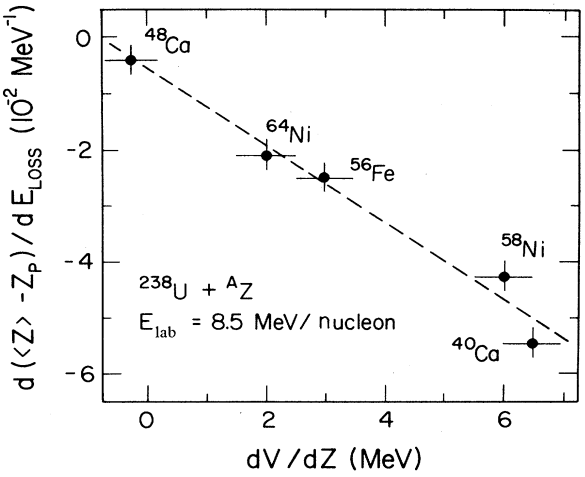

FIG. 21. Correlation of the slope of the proton drift as a function of energy loss (for energy losses less than 50 MeV) with the average slope of the potential energy per Z unit determined for the vicinity of the injection point.

the local gradient of the PES. As predicted by the reaction model, these second moments depend on the local curvatures of the PES, which are apparently rather independent of the projectile-target combination and are well represented by the liquid-drop energetics.

The experimental isobaric variances $\sigma_Z^2(A)$ are a factor of approximately four smaller than the isotopic variances $\sigma_A^2(Z)$. This difference reflects the fact that the restoring forces in the Z degree of freedom are larger than the restoring forces in the A degree of freedom. The correlation coefficient ρ_{NZ} increases with energy loss, revealing increasingly the influence of the underlying structure in the potential energy surface.

As expected, the extreme neutron richness of the ^{48}Ca projectile, along with the neutron-rich ^{238}U target, results in a secondary projectile-like product distribution that is markedly shifted to the neutron-rich side of the beta-stability line of projectile-like fragments. Several neutron-rich nuclides, first identified in the ^{238}U+^{56}Fe reaction, were also observed in the present reaction.

ACKNOWLEDGMENTS

It is due to the combined efforts of many persons, the administration, operations, and scientific support personnel associated with the Lawrence Berkeley Laboratory SuperHILAC facility, that the present reaction, involving a rare ^{48}Ca beam, could be added to the systematical study of transport phenomena in damped reactions. The authors acknowledge this with pleasure and appreciation. Thanks are due to Dr. I. M. Govil and Dr. W. P. Zank for their assistance during the experiment. This work was supported by the U.S. Department of Energy under Grant No. DE-FG02-88ER40414.

*Now at: National Superconducting Cyclotron Laboratory, Michigan State University, East Lansing, MI 48824.

[1]See W. U. Schröder and J. R. Huizenga, in *Treatise on Heavy-Ion Science,* edited by D. A. Bromley (Plenum, New York, 1984), Vol. 2, Chap. 3, pp. 115–734, and references cited therein.

[2]J. Randrup, Nucl. Phys. **A307**, 319 (1978); **A327**, 490 (1979); **A383**, 468 (1982).

[3]W. Nörenberg, Z. Phys. A **274**, 241 (1975); **276**, 84 (1976); in *Proceedings of the International Symposium on Continuum Spectra, San Antonio, 1979,* edited by T. Tamura, J. B. Natowtiz, and D. H. Youngblood (Harwood Academic, Chur, London, 1980), Vol. 2, p. 383.

[4]G. Guarino, A. Gobbi, K. D. Hildenbrand, W. F. J. Müller, A. Olmi, H. Sann, S. Bjørnholm, and G. Rudolf, Nucl. Phys. **A424**, 157 (1984).

[5]R. T. de Souza, J. R. Huizenga, W. U. Schröder, Phys. Rev. C **37**, 1901 (1988).

[6]R. T. de Souza, W. U. Schröder, J. R. Huizenga, R. Planeta, K. Kwiatkowski, V. E. Viola, and H. Breuer, Phys. Rev. C **37**, 1783 (1988).

[7]W. U. Schröder, J. R. Birkelund, J. R. Huizenga, K. L. Wolf, and V. E. Viola, Jr., Phys. Rep. **45**, 310 (1978).

[8]J. B. Moulton, J. E. Stephenson, R. P. Schmitt, and G. Wozniak, Nucl. Instrum. Methods **157**, 325 (1978).

[9]K. Braune, Ph.D. thesis, Max-Planck-Institut, 1978; D. Schwalm (private communication).

[10]D. Schwalm, A. Bamberger, P. G. Bizetti, B. Povh, G. A. P. Englebertink, J. W. Olness, and E. K. Warburton, Nucl. Phys. **A192**, 449 (1972).

[11]K. Warburton, J. W. Olness, and A. R. Poletti, Phys. Rev. **160**, 938 (1967).

[12]H. Breuer, A. C. Mignerey, V. E. Viola, K. L. Wolf, J. R. Birkelund, D. Hilscher, J. R. Huizenga, W. U. Schröder, and W. W. Wilcke, Phys. Rev. C **28**, 1080 (1983); H. Breuer, K. L. Wolf, B. G. Glagola, K. K. Kwiatkowski, A. G. Mignerey, V. E. Viola, W. W. Wilcke, W. U. Schröder, J. R. Huizenga, D. Hilscher, and J. Birkelund, Phys. Rev. C **22**, 2454 (1980).

[13]W. U. Schröder, J. R. Huizenga, J. R. Birkelund, K. L. Wolf, and V. E. Viola, Jr., Phys. Rev. C **16**, 623 (1977).

[14]J. Wilczyński, Phys. Lett. **47B**, 484 (1973).

[15]J. P. Bondorf, M. I. Sobel, and D. Sperber, Phys. Rep. **15**, 83 (1974).

[16]W. J. Myers and W. J. Swiatecki, Ark. Fys. **36**, 343 (1967).

[17]W. U. Schröder, J. R. Huizenga, and J. Randrup, Phys. Lett. **98B**, 355 (1981); W. U. Schröder (unpublished).

[18]W. U. Schröder, R. T. de Souza, J. R. Huizenga, and L. M. Schmieder, in *Proceedings of the International Symposium on Nuclear Fission Heavy-Ion Reactions,* Nuclear Science Research Conference Series **11**, 255 (1987).

[19]A. Gavron, Phys. Rev. C **21**, 230 (1980).

[20]H. Freiesleben and J. V. Kratz, Phys. Rep. **106**, 1 (1984).

[21]D. H. E. Gross and K. M. Hartmann, Phys. Rev. C **24**, 2526 (1981).